Article:
Shi, W., Li, C., Zhu, R. et al. (2026) Sulfate-driven phosphorus recycling and the collapse of lacustrine ecological diversity in the mid-Triassic. Earth and Planetary Science Letters, 691. 120198. ISSN: 0012-821X

https://doi.org/10.1016/j.epsl.2026.120198

Figures and captions

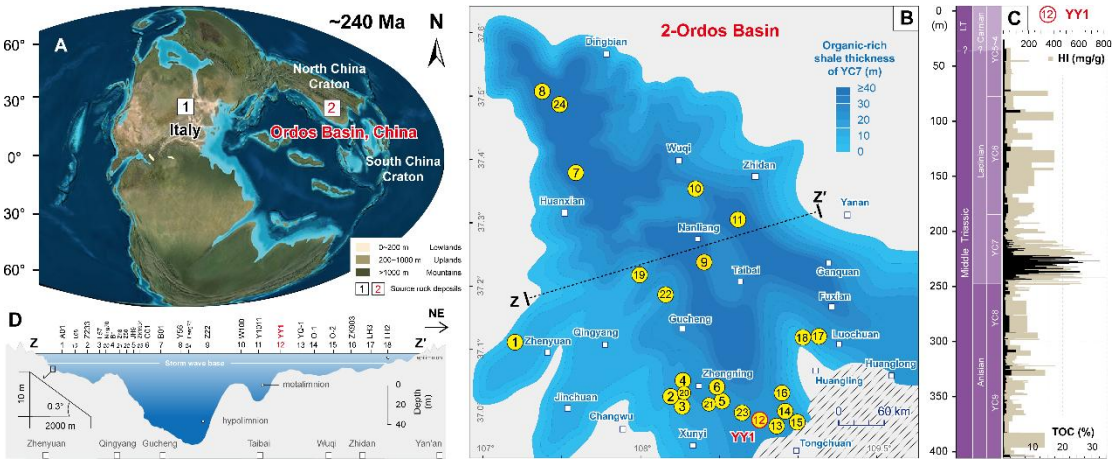

Fig. 1. Location and geological setting of the study sections. (A) Reconstructed Paleogeography of the late Middle Triassic at ~240 Ma, including the location of two major source rock deposits in Italy and North China. (B) Isopach map of the organic-rich shale of Member 7 of the Yangchang Formation (YC7) in the Ordos Basin, North China, including relative estimated water depths. Circles with number represent the 24 drillcores in this study, among which drillcore No. 12 is the YY1 drillcore. (C) Stratigraphic column of the Yangchang Formation in YY1, containing the distinguishable 'hot shale' of YC7 with high total organic carbon (TOC) and hydrogen index (HI) values. (D) East-west-oriented dip-line cross-section (Z to Z') in the Ordos Basin, with the relative position of the 24 drillcores.

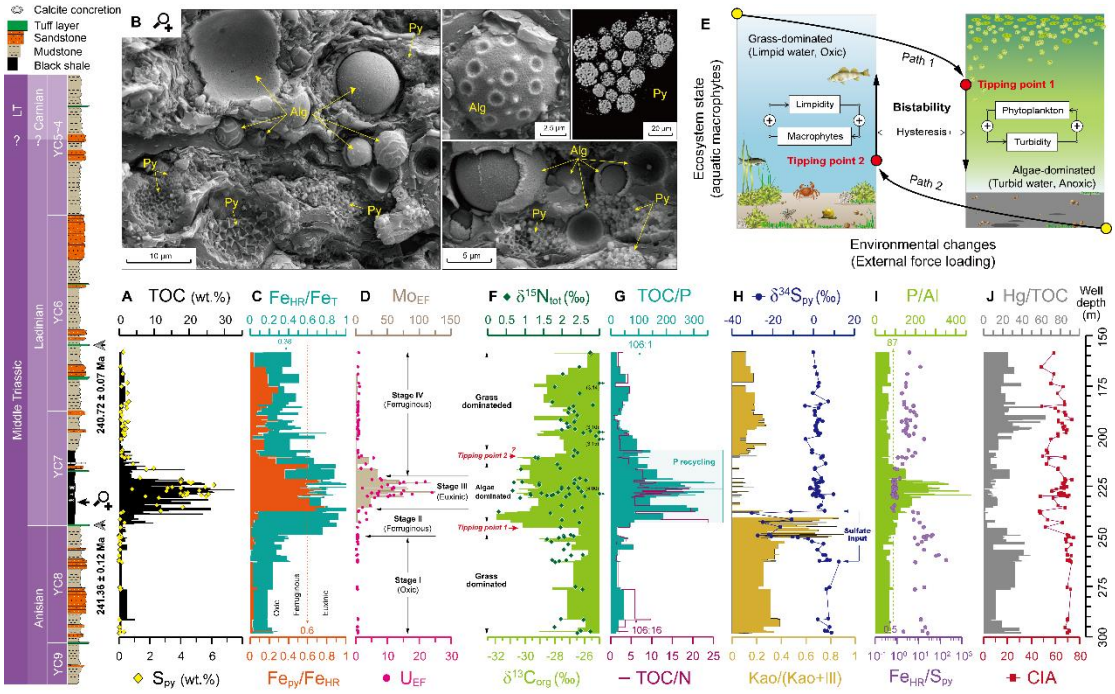

Fig. 2. Lithostratigraphy, geochronology and chemostratigraphy of the YY1 drillcore, Ordos Basin. (A) Concentration of total organic carbon (TOC) and pyrite sulfur (S_{py}). (B) Scanning electronic microscopy (SEM) images showing the coexistence of Chrysophyte fossils and pyrite framboids. Abbreviation: Alg, algae fossils; Py, pyrite framboids. (C) Iron speciation data. Dashed blue line on the Fe_{HR}/Fe_T plot represents the defined boundary for identifying oxic and anoxic deposition. The dashed red line on the Fe_{py}/Fe_{HR} plot distinguishes euxinic from ferruginous deposition (for samples clearly deposited from an anoxic water column). (D) Molybdenum (Mo_{EF}) and uranium (U_{EF}) enrichment factors. (E) Tipping points mark discontinuous changes in the state of an ecosystem. Alongside external force uploading, the initial grass-dominated ecosystem follows the equilibrium line (Path 1) until conditions cross Tipping Point 1, at which point the oxic, limpid water disappears and the ecosystem state drops abruptly to the algae-dominated stable state with anoxic, turbid-water. In turn, reducing external force—but to a much lower level—leads to the restoration of the grass-dominated stable state at the crossing of Tipping Point 2. The difference between the forward and backward tipping points marks the hysteresis in the system. For this range of conditions, the ecosystem can be found in either of the two alternative stable states (bistability). (F) Organic carbon isotope ($\delta^{13}C_{org}$) and bulk nitrogen isotope ($\delta^{15}N_{tot}$) values. (G) Mercury concentrations and Hg/TOC ratios. (H) Phosphorus concentrations normalized to aluminum (P/Al), and chemical index of alteration (CIA) values. (I) Molar TOC/P and N/P ratios. (J) Pyrite sulfur isotope ($\delta^{34}S_{py}$) values, and kaolinite normalized to the sum of kaolinite and illite [Kao/(Kao+Ill)] ratios.

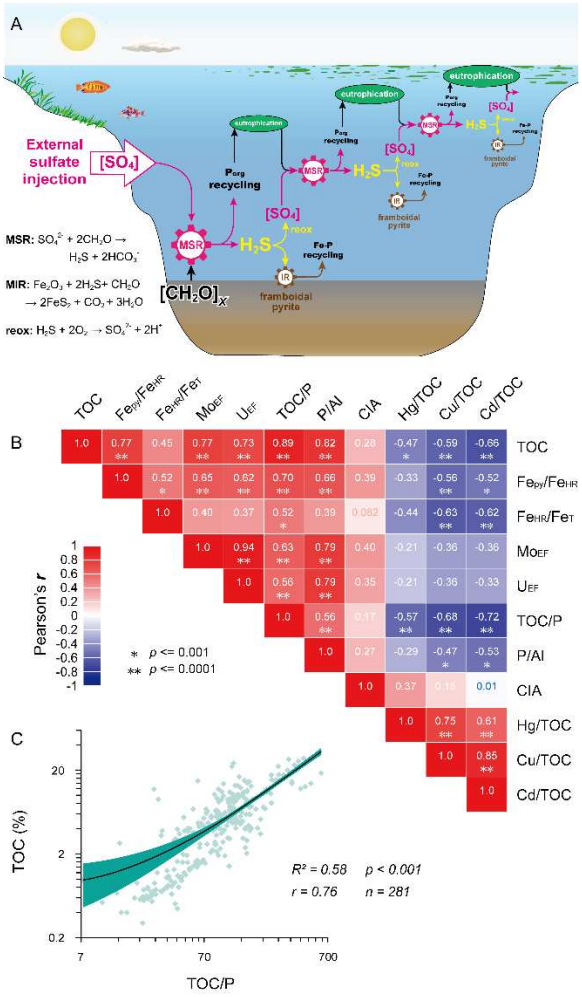

Fig. 3. Biogeochemical processes related to the development of sulfate-driven eutrophication in the paleolake (A), heat map showing the relationship between different geochemical variables (B), and data compilation analysis showing the correlation between TOC and TOC/P (C). In (A), organic carbon ($[CH_2O]_x$) is oxidized by microbial sulfate reduction (MSR) using external sulfate (sourced by volcanic sulfate aerosols and/or gypsum dissolution), during which organic phosphorus is released. Part of the derived H_2S stimulated iron reduction (IR) and pyrite formation, during which iron-bound phosphorus (Fe-P) is released. Recycled phosphorus promotes eutrophication, while residual H_2S in the water column may be re-oxidized back to sulfate to fuel the next circulation. In (B), with all data coming from the YY1 drillcore, TOC has a high correlation with TOC:P (0.89) and P/Al (0.82), a moderate correlation with euxinia (Fe_{py}/Fe_{HR} of 0.77, Mo_{EF} of 0.77 and U_{EF} of 0.73), but no correlation with weathering (CIA) and volcanic (heavy metals) proxies. In (C), paired TOC and TOC/P data for the YC7 organic-enriched shale are collected from the 18 contemporaneous drillcores.

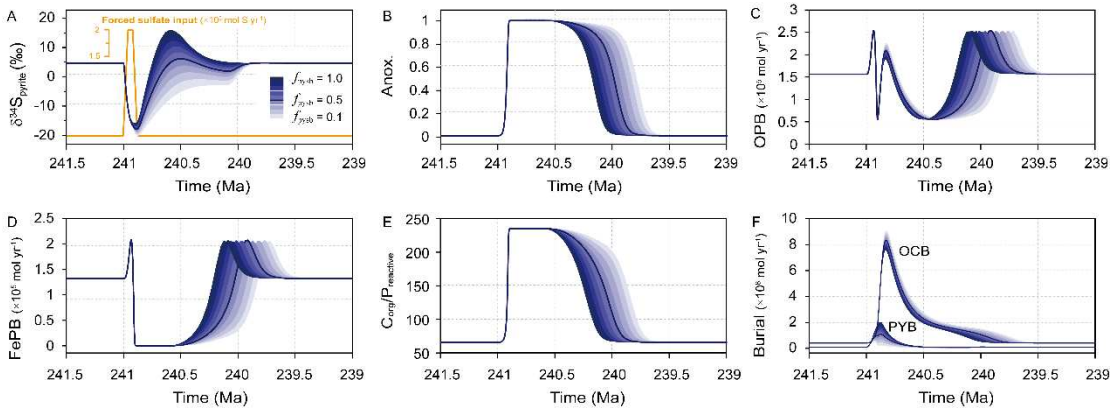

Fig. 4. COPSE biogeochemical model results for lacustrine redox and nutrient dynamics with a forced weathering sulfate input and varying fractions of pyrite burial. (A) Pyrite sulfur isotopes (given as $\delta^{34}S_{py}$). (B) Degree of water column anoxia. A value of 1 on the Y-axis means completely anoxic, while 0 means completely oxic. (C) Burial flux of iron-bound P. (D) Burial flux of organic P. (E) Calculated $C_{org}/P_{reactive}$, where $P_{reactive}$ is the sum of organic P, iron-bound P and authigenic P. (F) Burial fluxes of organic carbon (OCB) and pyrite sulfur (PYB).

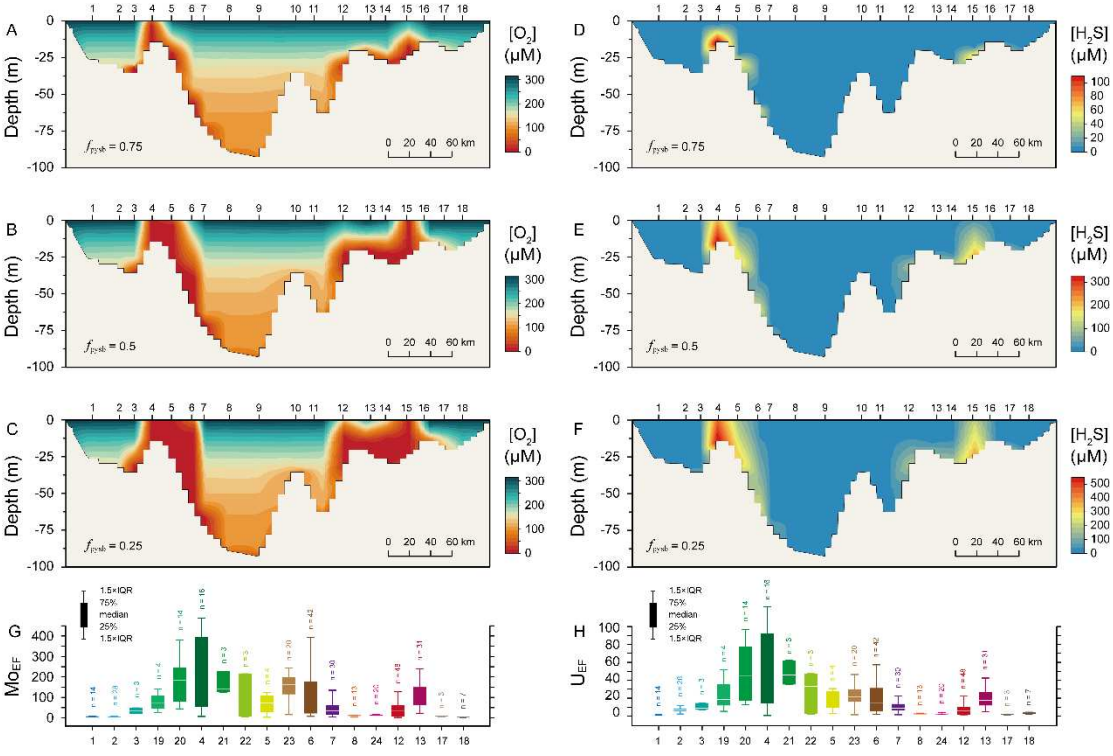

Fig. 5. Spatial visualization of dissolved oxygen and H_2S concentrations with varying fractions of pyrite burial (f_{pysb}) (A–F), and box plots of enrichment factors of redox sensitivity elements (i.e., Mo_{EF} and U_{EF}) (G–H) across an east-west-oriented dip-line in the Ordos Basin during deposition of YC7 organic-rich shale. A total of 1,100 C-S data from drillcores No. 1–18 were used to grid the [O_2]

(A-C; left) and [H_2S] (D-F; right) concentrations based on the Fike's Second Law and the Kriging interpolation method. A total of 606 Mo_{EF}–U_{EF} data from drillcores No. 1–8, 12–13, and 1724 (G–H) were used for verifiable comparison with the modelling results as shown in A–F. The boundary of YC6/YC7 was treated as a datum plane for all the locations (see Methods and Supplementary Materials for sample location and model details; Figs. S5 and S6; Table S5).

MATERIALS AND METHODS

Samples were collected from the 400-m-thick YY-1 drillcore located in the southeast Ordos Basin (Fig. 1A). The selected samples were subjected to detailed sedimentology and geochemistry, comprising TOC (n = 276), XRD of total rocks (n = 284) and clay minerals (n = 284), iron speciation (n = 93), major and trace element measurements (n = 93), total nitrogen (TN) and N isotopes ($\delta^{15}N_{total}$) (n = 93), Hg concentrations (n = 93), organic carbon isotopes ($\delta^{13}C_{org}$) (n = 93), and pyrite sulfur isotopes ($\delta^{34}S_{py}$) (n = 93). Two samples were also analyzed for U-Pb dating.

U-Pb dating

Samples YY1-T1 and YY1-T2 were collected for LA-MC-ICP-MS (laser ablation–multi-collector–inductively coupled plasma mass spectrometry) U-Pb dating via a Resonetics RESOlution M-50-HR excimer laser ablation system. Zircons from sample YY1-T1, at the base of the organic-rich shale of YC7, gave an age of 241.36 ± 0.12 Ma (2s). The second sample, YY1-T2, from the middle of YC6, yielded an age of 240.72± 0.07 Ma (2s). Integrating with previous age data, the lower and upper age limits of the YC7 organic-rich shale are 241.36 Ma and 241.0 Ma, respectively.

TOC and TN

TOC and TN were measured using an Elementar Vario EL cube EA with decarbonated samples. Quality control checks were performed on every 10th sample, including sample duplicates, analysis of certified reference materials (acetanilide), and analysis of blanks. The measurement precision was better than ±0.1 wt% for TOC and ±0.3 wt% for TN.

Iron speciation

The iron content in pyrite (Fe_{py}) was determined stoichiometrically based on the weight percentage of Ag_2S obtained through chromium reduction (*83*). For iron associated with carbonate, magnetite, and (oxyhydr)oxides, a sequential extraction procedure (*84*) was applied to approximately 0.1 g of powdered sample in 15-mL centrifuge tubes. The extraction sequence began with sodium acetate treatment at 50°C (pH=4.5, 48h) to isolate carbonate-bound iron (Fe_{carb}). The remaining solid was subsequently exposed to sodium dithionite at room temperature (pH=4.8, 2 h) to dissolve (oxyhydr)oxide phases (Fe_{ox}). Finally, magnetite (Fe_{mag}) was extracted using ammonium oxalate (room temperature, 6 h). Iron concentrations in all extracts were quantified via inductively coupled plasma optical emission spectrometry (ICP-OES, Agilent 710), achieving an analytical precision better than 5%.

Statistically, boundaries for distinguishing anoxic (Fe_{HR}/Fe_T >0.38) water column redox conditions were devised for marine settings (*85*) while a Fe_{py}/Fe_{HR} ratio above 0.7–0.8 is generally diagnostic of euxinic waters, where Fe_{HR} represents the combined pool of Fe_{py}, Fe_{carb}, Fe_{ox}, and Fe_{mag}. Although care is required when applying marine sediment iron speciation thresholds to lacustrine sediments, this approach has been well established to be used successfully in larger lacustrine settings, such as the Subei Basin (86), where the Fe shuttle that leads to Fe_{HR} enrichments under anoxic water conditions (*85–87*) may still operate (*88*). Low Fe_{py}/Fe_{HR} ratios (<0.6) then suggest that when anoxic, the water column was ferruginous rather than euxinic (*31,32,61*). Therefore, this threshold for euxinia was adjusted to 0.6 in this study.

Pyrite-S $\delta^{34}S$ analysis

Pyrite-S isotope ($\delta^{34}S_{py}$) analyses were performed on Ag_2S precipitates using an Elementar PYRO cube coupled to an IsoPrime continuous flow mass spectrometer. Laboratory standard SWS-3A ($BaSO_4$, $\delta^{34}S$ = +20.3‰), inter-laboratory standard CP-1 (chalcopyrite, $\delta^{34}S$ = −4.56‰), and international reference standard IAEA S-3 ($\delta^{34}S$

= −32.06‰) were used to check precision and accuracy. Replicate analyses of a laboratory $BaSO_4$ standard yielded an accuracy of <0.33‰, and a precision of <0.3‰ (1 σ) for $\delta^{34}S$.

Major and trace elements

Major and trace element concentrations in the SKL-G PMR samples were determined using a PANalytical Zetium X-ray fluorescence spectrometer and an Agilent 7500a inductively coupled plasma mass spectrometer (ICP-MS), respectively. For major element analysis, powdered samples were fused into glass beads and measured via wavelength-dispersive XRF. Trace element quantification involved acid digestion of sample powders with a mixture of HNO_3 and HF prior to ICP-MS measurement. Analytical precision, assessed through repeated measurements of certified reference materials (GBW07132, GBW07133, and GBW07407 for major elements; AGV-2, BHVO-2, BCR-2, and GSR-1 for trace elements), yielded relative standard deviations better than 5% for major elements and below 2% for trace elements.

The CIA parameter was calculated from the ratio of Al to major base oxides (*89,90*):

$$CIA = Al_2O_3 / (Al_2O_3 + K_2O + Na_2O + CaO^*) \times 100 \quad (1)$$

where all variables represent the molar amounts of major-element oxides. CaO* represents the fraction of CaO in silicate minerals, which is used in place of total CaO in order to avoid contributions of CaO from carbonate and phosphate minerals that are not tightly linked to weathering processes.

Enrichment factors (EFs) for trace elements were calculated as:

$$X_{EF} = (X/Al)_{sample} / (X/Al)_{AUCC} \quad (2)$$

where X is the element of interest (i.e., Mo and U), and AUCC is average upper continental crust (*91*).

Total rock $\delta^{15}N$ analysis

Nitrogen isotope compositions ($\delta^{15}N_{tot}$) were analyzed on two sample types:

decarbonated bulk sediment (40–80 mg) and isolated kerogen concentrates (~20 mg). Samples were combined with V_2O_5 catalyst, sealed in tin capsules, and combusted at 1020°C. The liberated CO_2 was trapped using an alkali lime absorption system. Isotopic values are reported in standard δ notation relative to atmospheric N_2 ($\delta^{15}N_{AIR}$ = 0‰). Calibration with international reference materials USGS40 ($\delta^{15}N_{AIR}$ = –4.52‰) and IAEA-N-2 ($\delta^{15}N_{AIR}$ = +20.3‰) confirmed analytical precision better than 0.5‰. Procedural blanks containing 10 mg V_2O_5 (Thermo Scientific, Cambridge, UK, PN 33837510) showed no detectable nitrogen signal.

Organic $\delta^{13}C$ analysis

For $\delta^{13}C_{org}$ determination, homogenized rock powder samples (5–50 g) were treated with 10% HCl at room temperature for 24 hours with periodic agitation. The supernatant pH was monitored during acid washing; additional acid was introduced if the pH approached neutral to ensure complete carbonate removal. After full dissolution, the residual solids were rinsed repeatedly with deionized water until neutral pH was achieved, and then oven-dried at 60 °C. Organic carbon isotope measurements were performed using a Flash EA2000 elemental analyzer coupled online to a Thermo Fisher MAT 253 isotope ratio mass spectrometer. Flash combustion and reduction furnace temperatures were maintained at 1050 °C and 680 °C, respectively. Calibration was conducted using certified standards GBW04407 ($\delta^{13}C_{org}$ = −22.4‰) and GBW04408 ($\delta^{13}C_{org}$ = −36.9‰). Analytical accuracy, verified through repeated standard and sample measurements, was better than ±0.1‰ (1σ).

Hg concentration analysis

Mercury content in solid samples was determined using a Lumex R-915F mercury analyzer. Samples were combusted at approximately 750 °C to release elemental mercury vapor, which was quantified by cold vapor atomic absorption spectroscopy (CV-AAS), with a method detection limit below 0.5 ng/g. Quality control was performed by repeated analysis of the certified reference material GBW07311 (GSD-

11, freshwater sediment). The measured average Hg concentration in GSD-11 was 72.2 ± 5.8 ng/g (2 SD, n = 8), consistent with the certified value of 72 ± 9 ng/g.

Mineral quantification and clay mineral analysis

Mineralogical composition was analyzed using a Kratos XRD-6000 diffractometer equipped with a Cu X-ray tube. Powdered samples, mixed with 10 wt% ZnO as an internal standard, were homogenized in a McCrone mill with methanol, dried, and side-loaded to minimize preferred orientation. XRD patterns were collected over a 2–65° 2θ range. Quantitative phase analysis was performed using the BGMN Rietveld refinement software and Quanta (Chevron), a modified reference intensity ratio and full-pattern fitting program. Based on tests with artificial mixtures, estimated uncertainties are approximately ±10 wt% for clay minerals and ±5 wt% for major mineral phases. Clay mineral characterization was based on XRD and compositional data from 30 clay-sized fractions isolated from representative samples. Sample pretreatment included removal of carbonates, organic matter, and Fe/Mn (oxyhydr)oxides. The <0.5 μm fraction was separated by centrifugation, deposited as oriented aggregates on glass slides, and analyzed under air-dried and ethylene-glycol-saturated conditions across 1.5–30° 2θ. Select samples were side-packed to assess *hkl* reflections for octahedral site occupancy determination. Scanning electron microscopy (SEM) was used to examine mineral textures and paragenesis in polished and fractured samples. Bulk chemical composition of clay separates was obtained via energy-dispersive X-ray spectroscopy (EDS) on samples mounted on conductive tape.

Geochemical modeling in temporal dimension

The geochemical model used in this study was designed based on the COPSE (Carbon Oxygen Phosphorus Sulfur Evolution) model, which includes a series of biogeochemical processes operating on a nutrient-driven ecosystem that is sufficiently generalized to allow many different hypotheses to be tested and compared by including different proposed flux functions and changing parameters (*59*). Within this framework,

the original COPSE model treated the water (i.e., ocean) and surface sediment as a well-mixed single box that can be applied to geochemical simulations of homogeneous, enclosed systems such as lakes without regard to density stratification (Fig. S4). Here, we reasonably shrink oceanic reservoirs (e.g., carbon, sulfur and phosphorus) and fluxes (weathering, degassing and burial) by seven orders of magnitude to match the size of the Ordos Basin, while keeping atmospheric oxygen and carbon dioxide levels at steady state (i.e., pO_2 = 1 PAL and pCO_2 = 1 PAL, where PAL = present atmospheric level) during the model runs. See Tables S1–S4 for a full model description.

We first ran the COPSE model for 0.5 million years to a 'Triassic-like' steady state characterized by $[SO_4^{2-}]$ = 2 mM, which was achieved by adjusting the gypsum burial rates. Note that the initial steady state of $[SO_4^{2-}]$ = 2 mM is regarded as the requirement for a small $\triangle^{34}S$ (*46,47*) as implied by high $\delta^{34}S_{py}$ (e.g., ~5‰ in YC8). According to $\delta^{34}S_{py}$ and Kao/(Kao+Ill) records, we imposed a forced sulfate input (S_{input}) lasting for 0.1 Myr coincident with the observed negative $\delta^{34}S_{py}$ excursion, to examine lacustrine redox and nutrient dynamics:

$$S_{input} = interp1([241.5\ 241\ 240.95\ 240.9\ 240.85\ 239], [1\ 1\ x\ x\ 1\ 1], t) \quad (3)$$

where interp1 represents a 1-dimensional interpolation, and the following vectors in brackets in Eq. (3) are the interpolation points for time (in Myr) relative to the start of YC7 deposition at ~241 Ma, and the multiples of an external sulfate input (x) relative to the background sulfate weathering flux (2×10^5 mol S yr^{-1}), respectively. We assume the MSR rate (F_{MSR}) is coupled with the relative sulfate level as follows:

$$F_{MSR} = k_{MSR} \cdot \frac{S_t}{S_0} \quad (4)$$

where k_{MSR} is the rate constant of MSR, and S_t and S_0 are the masses of the lacustrine sulfate reservoir at time t and at start (0), respectively. For the model run, a partitioning constant f_{pysb} was used to determine what fraction of MSR-derived H_2S was buried as pyrite:

$$PYB = F_{MSR} \cdot f_{pysb} \quad (5)$$

where PYB is the burial flux of pyrite. MSR-derived H_2S that is not buried as pyrite is assumed to be re-oxidized into sulfate, and return to the water sulfate reservoir. To

model the effect of MSR on P recycling, we denoted $P_{recycle}$ as the flux of organic P recycled, which is coupled with the F_{MSR}:

$$P_{recycle} = \frac{F_{MSR}}{k_{SP}} \quad (6)$$

where $k_{SP} = 53$ is the S/P molar ratio of MSR according to the Redfield Ratio of C/P = 106/1 in marine algal biomass. S isotope data from modern, low-sulfate euxinic systems illustrate that MSR-induced S-isotopic fractionation values (ε_{SR}) are positively correlated with sulfate concentration. To model the influence of increased sulfate concentration on ε_{SR}, we applied the following empirical equations (*47*):

$$\Delta^{34}S = 7.03 \cdot \ln([SO_4^{2-}]) + 21.22 \quad (7)$$

$$\varepsilon_{SR} = (\Delta^{34}S + 9.54)/1.09 \quad (8)$$

Geochemical modeling in spatial dimension

The spatial redox variation across the Ordos Basin was modelled using a one-dimensional, depth-dependent geochemical model based on Fike's Second Law, in which the [O_2] (and [H_2S]) vary with time (t) according to physical processes (i.e., diffusion and advection), and further considering depth-dependent rates of respiratory O_2 demand and H_2S oxidation. For simplicity, we make the following premises: (i) diffusivity and advection constants are constant with depth, (ii) the water column is relatively motionless on the modelled timescale (Myr), whereas gas transport is controlled only by diffusion and advection, without influence from large storms or upwelling, (iii) H_2S oxidation generates sulfate and not intermediate sulfur species, (iv) the background climatic factors including atmospheric oxygen, carbon dioxide levels and water temperature (T) are kept unchanged (i.e., pO_2 = 1 PAL; pCO_2 = 1 PAL; T = 20 ℃) to exclude the possible influence of global climate variability. The solute flux for dissolved oxygen at depth *x* is described as follows:

$$\frac{\partial O_2}{\partial t} = D_1 \frac{\partial^2 O_2}{\partial x^2} - v\frac{\partial O_2}{\partial x} - kexp\left[-\left(\frac{k}{v}\right)x\right] \quad (9)$$

where D_1 is the diffusion coefficient of molecular oxygen, *v* is the advective velocity, and *k* is the rate constant for microorganism respiration. H_2S diffuses bottom-up and its solute flux for H_2S at depth *x* is given as follows:

$$\frac{\partial H_2S}{\partial t} = D_2 \frac{\partial^2 H_2S}{\partial (d-x)^2} - v \frac{\partial H_2S}{\partial (d-x)} \quad (10)$$

where D_2 is the diffusion coefficient of molecular H_2S and d is the real depth of a given section. We defined the H_2S reoxidation process as the difference between $[O_2]$ and $[H_2S]$, thus the real concentration of $[O_2]$ at depth x is calculated as follows:

$$[O_2]_x = \begin{cases} \int_0^x \frac{\partial O_2}{\partial t} - 2 \cdot \int_d^{d-x} \frac{\partial H_2S}{\partial t}, if \int_0^x \frac{\partial O_2}{\partial t} > 2 \cdot \int_d^{d-x} \frac{\partial H_2S}{\partial t} \\ 0, \qquad\qquad if \int_0^x \frac{\partial O_2}{\partial t} < 2 \cdot \int_d^{d-x} \frac{\partial H_2S}{\partial t} \end{cases} \quad (11)$$

and the real concentration of $[H_2S]$ at depth x equals to:

$$[H_2S]_x = \begin{cases} 2 \cdot \int_d^{d-x} \frac{\partial H_2S}{\partial t} - \int_0^x \frac{\partial O_2}{\partial t}, if \int_0^x \frac{\partial O_2}{\partial t} < 2 \cdot \int_d^{d-x} \frac{\partial H_2S}{\partial t} \\ 0, \qquad\qquad if \int_0^x \frac{\partial O_2}{\partial t} > 2 \cdot \int_d^{d-x} \frac{\partial H_2S}{\partial t} \end{cases} \quad (12)$$

In this approximation, the $[O_2]$ at surface layer (i.e., $[O_2]_0$) is ~325 μM according to a given pO_2 = 1 PAL, while the initial $[H_2S]$ (i.e., $[H_2S]_d$) is defined to be positively correlated with the benthic rate of MSR (F_{MSR}), which is calculated from collected TOC-S_{py} data of the 18 studied cores/sections (see Fig. S5 and Supplementary for more details). The F_{MSR} is modified from ref. (*63*) as follows:

$$F_{MSR} = \varphi \cdot \left(TOC + \frac{S_{py}}{2}\right) \cdot \frac{{S_{py}}^{\alpha}}{f_{pysb}} \quad (13)$$

where φ is the average benthic MSR rate in modern, anoxic lakes, α has been taken as 0.3 (*63*), and f_{pysb} is allowed it to range from 0.1 to 1 for the sensitivity experiments.

Kriging spatial interpolation. To map the two-dimensional distribution of modeled $[O_2]$ and $[H_2S]$ across the YC7 Ordos Basin, we carry out a best linear unbiased prediction using the Kriging Spatial Analyst, which determines a spatial autocovariance optimal interpolation method in the field of geostatistics:

$$\gamma(h) = \frac{1}{2N(h)} \sum_{i=1}^{N(h)} [Z(x_i) - Z(x_i + h)]^2 \quad (14)$$

where h is the spatial lag distance, $N(h)$ is the logarithmic quantization of samples with distance h, and $Z(x)$ is the $[O_2]$ and $[H_2S]$ value at site x.